*Article*

*J. Mex. Chem. Soc.* **2025**, *69*(1)
Special Issue

ISSN-e 2594-0317

# Kinetic Modelling of Anisole Hydrodeoxygenation Using Aromatic-Selective $Ru/TiO_2$ Catalyst

V. Martinez-Jimenez[1], Reyna Ríos-Escobedo[1], J. Gabriel Flores[2,3], Cindy García-Mendoza[1], Julia Aguilar Pliego[2*], José Antonio de los Reyes[1*], V.A. Suárez-Toriello[3,*]

[1]Universidad Autónoma Metropolitana–Iztapalapa, División de Ciencias Básicas e Ingeniería, Av. FFCC R. Atlixco 186, Col. Vicentina, 09340 Iztapalapa, CDMX, México.
[2]Área de Química Aplicada, Departamento de Ciencias Básicas, Universidad Autónoma Metropolitana-Azcapotzalco, 02200, Ciudad de México, México.
[3]CONAHCYT–UAM, Universidad Autónoma Metropolitana–Iztapalapa, Departamento de Ingeniería de Procesos e Hidráulica, Av. FFCC R. Atlixco 186, 09340 Iztapalapa, CDMX, México.

***Corresponding authors:** Julia Aguilar Pliego, email: apj@azc.uam.mx; José Antonio de los Reyes, email: jarh@xanum.uam.mx; V.A. Suárez-Toriello, email: vsuarezt@conahcyt.mx

Received May 24th, 2024; Accepted September 26th, 2024.

DOI: http://dx.doi.org/10.29356/jmcs.v69i1.2290

**Abstract.** A Langmuir-Hinshelwood kinetic model is proposed to describe the anisole hydrodeoxygenation over a $Ru/TiO_2$ catalyst in a continuous fixed-bed reactor. Key operating parameters, such as pressure, temperature, and weight hourly space velocity, were studied to ensure operation within the kinetic regime. The proposed kinetic model was successfully validated, and two adjacent catalytic sites were considered: one dedicated to the dissociative adsorption of hydrogen and the other to the adsorption and reaction of anisole and its reaction products. The model demonstrated a good fit with the experimental data, revealing a preference for the demethoxylation pathway leading to benzene formation over the demethylation pathway, which favors phenol formation. Characterization of the $Ru/TiO_2$ catalyst using XRD, TPR-$H_2$, TPD-$NH_3$, and XPS revealed the presence of highly dispersed Ru particles and oxophilic sites, including both acidic sites and oxygen vacancies, validating the two-site model. The kinetic parameters indicated that the conversion of cyclohexanol to cyclohexane was the fastest reaction step, and the demethoxylation pathway was favored over the demethylation on the $Ru/TiO_2$ catalyst.
**Keywords:** Kinetic modeling; hydrodeoxygenation; anisole; demethoxylation; demethylation; Ru; $TiO_2$.

**Resumen.** Se propone un modelo cinético Langmuir-Hinshelwood para describir la reacción de hidrodesoxigenación de anisol utilizando un catalizador $Ru/TiO_2$ en un reactor de flujo continuo de lecho fijo. Se evaluaron inicialmente las condiciones de operación, como la presión, temperatura y velocidad espacial, con el fin de asegurar que el sistema opere dentro del régimen cinético. El modelo considera la presencia de dos sitios catalíticos adyacentes: uno destinado a la adsorción disociativa del hidrógeno y otro para la adsorción y reacción tanto de anisol como de sus productos de reacción. El modelo mostró un buen ajuste con los datos experimentales, indicando una ruta preferencial hacia la desmetoxilación, que produce benceno, frente a la desmetilación, que favorece la formación de fenol. La caracterización del catalizador $Ru/TiO_2$ mediante técnicas de XRD, TPR-$H_2$, TPD-$NH_3$ y XPS reveló la presencia de partículas de $Ru^0$ altamente dispersas y sitios oxofílicos superficiales, incluidos sitios ácidos y vacantes de oxígeno, lo que valida el uso del modelo de dos sitios propuesto. Los parámetros cinéticos indicaron que la conversión de ciclohexanol a ciclohexano es el paso de reacción más rápido, y se favoreció la ruta de desmetoxilación sobre la desmetilación en presencia del catalizador $Ru/TiO_2$.

ISSN-e 2594-0317

**Palabras clave:** Modelado cinético; hidrodesoxigenación; anisol; desmetoxilación; desmetilación; Ru; $TiO_2$.

## Introduction

The global population has steadily increased in recent years, driving a growing demand for fossil fuels and an increasing dependence on non-renewable resources like oil, coal, and natural gas [1]. This rapid consumption leads to resource depletion and poses significant challenges in maintaining fossil fuel quality. Furthermore, conflicts over oil reserves, rising greenhouse gas emissions, and environmental pollution have intensified the search for alternative energy sources. Second-generation renewable fuels derived from non-edible biomass sources, such as agricultural, forestry, and other organic residues present a viable solution [2]. These alternatives are environmentally friendly, sustainable, and potentially cost-effective in the medium term. Additionally, being derived from biomass, these bioresources are integrated into the carbon cycle and are cleaner than petroleum-based products, containing less than 1 wt.% of nitrogen and sulfur [2-5].

Various thermochemical processes, such as pyrolysis, gasification, and liquefaction, can convert biomass into fuels and chemical products [4,5]. These processes produce bio-oils from the lignin fraction of lignocellulosic biomass, rich in phenolic and other oxygenated aromatic compounds, making them potential analogs to petrochemical feedstocks. However, the high oxygen content in bio-oils causes instability and makes them prone to polymerization, significantly reducing their energy content [4,6,7]. Upgrading these bio-oils into usable fuels relies on hydrodeoxygenation (HDO) processes, which require catalysts that are not only active and selective but also stable enough to remove heteroatomic oxygen while increasing the value of aromatic products [8]. Early efforts employed commercial $MoS_2$-based hydrotreating catalysts, but these suffered from rapid deactivation due to coke formation, water-induced $MoS_2$ phase deactivation, and a tendency to produce fully hydrogenated products [8-12]. Similarly, transition metal-based catalysts, such as reduced nickel, could also suffer from deactivation issues [13, 14]. Recent studies have explored noble metal-based catalysts with low oxidation states, which, under certain conditions, have demonstrated high selectivity for the hydrogenolysis of C–O bonds in lignin-derived oxygenates while preserving the aromatic character of the deoxygenated molecules, although both aromatic and saturated ring products are still formed [15-18].

Several studies have emphasized the exceptional performance of the $Ru/TiO_2$ catalytic system in hydrodeoxygenation of phenolic compounds [13,19-22]. For instance, Shu et al. [21] investigated the role of various metals (Cu, Ni, Mo, Pd, Pt, and Ru) supported on $TiO_2$ in the guaiacol hydrodeoxygenation. Among these, $Mo/TiO_2$, $Pt/TiO_2$, and $Ru/TiO_2$ catalysts demonstrated superior catalytic activity. Notably, $Pt/TiO_2$ and $Ru/TiO_2$ exhibited remarkable selectivity towards cyclohexane (74.4 and 91.3 %, respectively), whereas $Mo/TiO_2$ catalyst achieved only 4.7 %. In comparison, for phenol HDO, $Ru/TiO_2$ was 6.5 and 2 times more active than $Ru/ZrO_2$ and $Ru/Al_2O_3$, respectively, displaying high selectivity towards fully deoxygenated products [13]. Furthermore, Boonyasuwat et al. [23] evaluated the effect of different supports ($TiO_2$, $Al_2O_3$, $SiO_2$, and C) on Ru-based catalysts, concluding that the $Ru/TiO_2$ catalyst presented superior performance. The outstanding performance of the $Ru/TiO_2$ catalytic system has been attributed to the synergistic ability of Ru to dissociate hydrogen and the oxophilic nature (acidic sites and oxygen vacancies) of the $TiO_2$ support, which is capable of absorbing oxygen molecules [6,7,24]. Therefore, he capacity of $Ru/TiO_2$ to cleave the C–O bonds in phenolic molecules is due to the hydrogen spillover effect from $Ru^0$ onto the $TiO_2$ support, where $Ti^{3+}$surface sites promotes hydrogenolysis [19,20,22,25]. This effect is predominantly observed in catalysts with high Ru dispersion.

Previous studies have examined the kinetics of anisole hydrodeoxygenation (HDO) using simple power-law models for Pt and Ni catalysts [26,27]. Lee et al. [28] studied the anisole hydrodeoxygenation to benzene over a $Mo_2C$ catalyst at low temperatures (420−520 K), finding zero-order kinetics for anisole. Three primary pathways for anisole HDO have been identified: (i) demethoxylation (DMO) [29,30], (ii) demethylation (DME) [15,31], and (iii) initial hydrogenation followed by subsequent deoxygenation (HYD) [15,32]. However, these simple kinetic models do not fully capture the complexities of the reaction mechanism involved in HDO processes over heterogeneous catalysts. A deeper understanding of the reaction mechanisms and kinetics remains necessary to optimize catalyst

ISSN-e 2594-0317

design and process conditions [29]. Hydrotreatment reactions typically follow a Langmuir-Hinshelwood model, which assumes (i) dissociative adsorption of hydrogen, (ii) equivalence and independence of adsorption sites, and (iii) the surface reaction as the rate-determining step [15,33-35]. For instance, Lee et al. [28] proposed a two-site kinetic model for anisole HDO to benzene, where $H_2$ dissociates on one site (S1) while anisole adsorbs on another site (S2). The dissociated hydrogen first binds to the oxygen atom of the adsorbed anisole, promoting phenolic C–O bond cleavage and producing methanol and benzene as end products. In the context of anisol HDO over $Ru/TiO_2$ catalysts, the interaction between highly dispersed $Ru^0$ nanoparticles (metallic sites) and oxophilic sites (oxygen vacancies and acidic sites) on the $TiO_2$ supports favors the adsorption and activation of both hydrogen and oxygenated compounds, facilitating deoxygenation [15,36]. The structural characterization of the $Ru/TiO_2$ catalysts, as shown in previous studies, reveals that the combination of these two types of catalytic sites enables a dissociative adsorption mechanism for anisole and other oxygenated compounds, optimizing their conversion toward deoxygenated products [36]. Therefore, a Langmuir-Hinshelwood kinetic model is suitable for describing the heterogeneous catalytic reactions occurring on $Ru/TiO_2$ catalyst during anisol HDO, considering the competitive adsorption at different active sites. This model can provide a more accurate representation of the reaction kinetics and mechanisms involved, aiding in developing predictive models for process optimization.

A deeper understanding of reaction kinetics in hydrogenation reactions is crucial for developing predictive models that enhance the design and optimization of chemical processes and elucidate catalyst functionalities for bio-oil upgrading [29]. However, the HDO reaction mechanism on supported metal catalysts remains poorly understood, requiring further exploration with robust kinetic models that account for the specific interactions between reactants and catalyst sites. This work focused on the anisole HDO over a $Ru/TiO_2$ catalyst, employing a Langmuir-Hinshelwood kinetic model to describe the reaction mechanism. By considering two types of catalytic sites –metallic Ru sites for hydrogen activation and oxophilic sites on $TiO_2$ for anisole adsorption– this work aims to determine the kinetic parameters that govern the reaction. Reactivity studies were performed using a liquid-phase anisole solution under $H_2$-high pressure (40 bar) and 300 °C. The proposed kinetic model provides a quantitative framework to interpret the experimental data and elucidate the HDO reaction mechanisms, aiming for improved aromatic selectivity. The $Ru/TiO_2$ catalyst was characterized using XRD, TPR-$H_2$, TPD-$NH_3$, and XPS to confirm the presence of both Ru metallic and oxophilic sites necessary for facilitating the anisole HDO reaction and validating the two-site model.

## Experimental

### Catalysts preparation

A $Ru/TiO_2$ catalyst was synthesized using commercial $TiO_2$ support (Degussa P-25; 56 $m^2 \cdot g^{-1}$; 80-100 mesh particle size) and ruthenium(III) nitrosyl nitrate ($Ru(NO)(NO_3)_3$; Sigma Aldrich) as the Ru precursor. Ru aqueous solution was incorporated into $TiO_2$ by incipient wetness technique to achieve a nominal 0.5 wt.% Ru. The sample was aged overnight at atmospheric conditions and then dried at 120 °C for 24 h. Calcination of the catalyst was intentionally omitted to avoid sintering [37] and volatilization of the Ru precursor [38].

### Catalysts characterization

X-ray diffraction (XRD) was performed using a Bruker D8 Advance diffractometer with CuKα radiation (λ =0.154051 nm) at 40 kV and 30 mA. Measurements were taken over a 2θ angle range from 5 to 70°, with a scanning rate of 0.01 ° $s^{-1}$. XRD analysis identifies the crystalline phases in the catalysts, providing insights into the overall structure and the metal dispersion.

The reducibility and surface acidity of the catalyst were determined using an Altamira Instrument AMI-90 equipped with a thermal conductivity detector (TCD). Reducibility was evaluated through temperature-programmed reduction with hydrogen (TPR-$H_2$). Approximately 50 mg of the $Ru/TiO_2$ catalyst sample was placed in a 4 mm ID quartz reactor and pre-treated at 120 °C for one hour under argon flow to remove moisture and adsorbed compounds. The reduction stage was performed under a constant flow of 10 vol.% $H_2$ (argon balance) at 50 $mL \cdot min^{-1}$, with linear heating from 50 to 900 °C at 10 °C $min^{-1}$. TPR-$H_2$ analysis helps determine the reducibility of the catalyst, indicating the presence of metal oxide species that can be reduced to form metal-active sites.

ISSN-e 2594-0317

The total surface acidity was determined by the temperature-programmed desorption of ammonia (TPD-$NH_3$). About 100 mg of catalyst was loaded into the reactor and pre-treated equivalently to TPR-$H_2$ analysis. The pre-treated catalyst was reduced at 350 °C under $H_2$ flow, then heated to 500 °C and cooled to 100 °C in He flow (10 °C $min^{-1}$). The sample was subsequently saturated with 5 mol.% $NH_3$ (helium balance) for 30 min. The desorption step was performed from 100 to 600 °C at 10 °C·$min^{-1}$ in He flow. The surface acid concentration was determined by integrating the area under the curve and using calibration pulses. TPD-$NH_3$ analysis provides information on the acidic properties of the catalyst, indicating the presence of acid sites.

The X-ray photoelectron spectroscopy (XPS) analyses for freshly reduced catalyst were performed using a PHI5000 Versa Probe II, Scanning XPS Microprobe (Physical Electronics) with monochromatic AlKα radiation (1486.6 eV, 150 W). Binding energies (BE) were corrected for charging effects using C 1s (284.8 eV) as a reference. The O 1s and Ru 3p spectra were Shirley background subtracted and decomposed using 30/70 Gaussian/Lorentzian parameters. Samples were reduced ex-situ in $H_2$ flow (60 mL·$min^{-1}$) at 350 °C and then charged into the sample holder, avoiding air contact. XPS analysis allows qualitative identification of surface element chemical states and composition, which validate the presence of both Ru-metallic and oxophilic sites proposed in the two-site model.

## Activity measurements

### Catalyst activation

The $Ru/TiO_2$ catalyst (80-120 mesh particle size) was activated in-situ in a packed-bed flow reactor (316L SS, 0.6 cm OD, and 28 cm length) at 350 °C for 3 h. The catalyst was mixed with inert silica carbide (100 mesh particle size) to ensure proper distribution and packing. A schematic diagram of the flow system, including a detailed catalytic packed-bed, is illustrated in Fig. 1. The catalyst was heated at a rate of 5 °C $min^{-1}$ under a flow of $H_2$ (100 mL•$min^{-1}$) at atmospheric pressure. Following the activation step, the reduced catalyst was allowed to cool in the $H_2$ atmosphere to avoid oxidation until the reaction started.

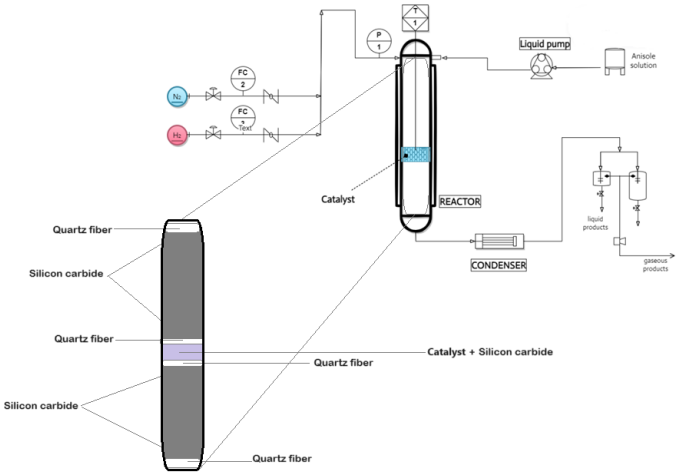


**Fig. 1.** Scheme of the high-pressure fixed bed reaction system used for the catalytic evaluation in the anisole HDO reaction.

## Catalytic evaluation in the HDO reaction of anisole

The catalytic activity of the reduced $Ru/TiO_2$ catalyst was evaluated through the anisole hydrodeoxygenation (HDO) reaction. The reaction was performed in a high-pressure fixed-bed reactor (Fig. 1). About 50 mg of catalyst (CAT) was in-situ reduced as previously described. The reactive mixture consisted of 0.2 mol $L^{-1}$ of anisole (A: $C_7H_8O$: 99 %; ~4,100 ppm O) dissolved in n-hexadecane ($C_{16}H_{34}$; >99 %); *n*-dodecane ($C_{12}H_{26}$; >99 %; 0.2 M) was used as internal standard. Before the catalytic evaluation, the reaction system was heated and stabilized at the reaction temperature and $H_2$ pressure.

*J. Mex. Chem. Soc.* **2025**, *69*(1)
Special Issue

ISSN-e 2594-0317

The effect of weight hourly space velocity (WHSV: 1.0 - 20.0 $g_A \cdot (g_{CAT} \bullet h)^{-1}$) was assessed by varying the reactor´s volumetric flow ($mL \bullet h^{-1}$) at different temperatures (200-300 °C) and 40 bar of $H_2$. The influence of reaction temperature (200, 250, and 300 °C) was evaluated at a WHSV of 15.3 $g_A \bullet (g_{CAT} \bullet h)^{-1}$ and 40 bar $H_2$. The effect of H2 pressure (30-50 bar) was also determined at 300 °C. Each operation condition was maintained for 4 h to reach the pseudo-steady state. The catalytic activity was expressed in terms of the reaction rate, defined as moles of anisole converted per gram of catalyst per second of reaction ($mol_A \bullet (g_{CAT} \bullet s)^{-1}$).

Reagents and products were identified, analyzed, and quantified using an Agilent 7890A gas chromatograph equipped with a flame ionization detector (FID) and a CP-Sil 5 CB column (60 m x 0.32 mm x 1.0 µm). Calibration curves were developed using the internal standard method to determine the molar concentration of the compounds: anisole (A), benzene (B), phenol (P), cyclohexane (CHA), cyclohexene (CHE), cyclohexanol (CHOL), and methylcyclohexane (MTCH). Total HDO conversion was calculated from the occurrence of output flow compound, and the production of B was considered the selectivity to the DMO route, while the production of CHOL, CHA, CHE, and MTCH represented the HYD routes. Conversion ($X_A$; Eq. 1) and yield ($Y_i$; Eq. 2) were calculated as follows [39]:

$$X_A = \frac{\sum n_{Products}}{n_A + \sum n_{Products}} \qquad \text{Eq. 1}$$

$$Y_i = \frac{n_i}{n_A + \sum n_{Products}} \qquad \text{Eq. 2}$$

**Determination of kinetic parameters: Theoretical model of two L-H type sites**

A rate expression based on the conventional L-H model was derived from the reaction network with the following assumptions:

I. Competitive molecular adsorption of the anisole and each hydrocarbon product in the reaction network (see Fig. 2) occurs at the same catalytic site.
II. Adsorption of water ($H_2O$) and methanol ($CH_3OH$) is negligible, as proposed by similar work [15].
III. Dissociative hydrogen adsorption occurs on metal sites that do not compete with the adsorption sites for anisole molecules and reaction products [34,40]. Consequently, hydrogen adsorption can be considered independent at different sites (S1 and S2), as summarized in the sequence of elementary steps presented in Table 1and based on the proposed anisole reaction network (Fig. 2). These assumptions are divided from the reaction products observed by GC analysis and model considerations.

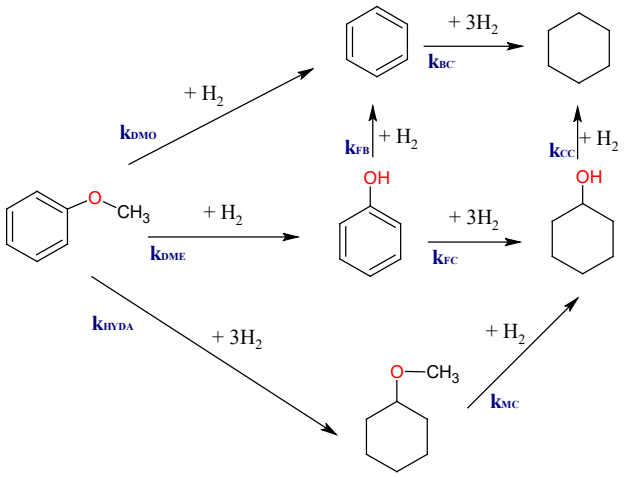


**Fig. 2.** Proposed reaction network scheme for anisole HDO at 200-300 °C and 30-50 bar ($P_{H2}$).

ISSN-e 2594-0317

**Table 1.** Elementary steps for anisole HDO on $Ru/TiO_2$ catalyst.

| Adsorption/Desorption | Reactions |
|---|---|
| $A + S_1 \overset{K_A}{\leftrightarrow} A - S_1$ | $A - S_1 + 2H - S_2 \overset{k_{DMO}}{\longrightarrow} B - S_1 + CH_3OH + 2S_2$ |
| $B + S_1 \overset{K_B}{\leftrightarrow} B - S_1$ | $A - S_1 + 6H - S_2 \overset{k_{HYDA}}{\longrightarrow} MTCH - S_1 + 6S_2$ |
| $CHA + S_1 \overset{K_{CHA}}{\longleftrightarrow} CHA - S_1$ | $A - S_1 + 2H - S_2 \overset{k_{DME}}{\longrightarrow} P - S_1 + H_2O + 2S_2$ |
| $MTCH + S_1 \overset{K_{MTCH}}{\longleftrightarrow} MTCH - S_1$ | $B - S_1 + 6H - S_2 \overset{k_{BC}}{\longrightarrow} CHA - S_1 + 4S_2$ |
| $CHOL + S_1 \overset{K_{CHOL}}{\longleftrightarrow} CHOL - S_1$ | $MTCH - S_1 + 2H - S_2 \overset{k_{MC}}{\longrightarrow} CHOL - S_1 + CH_4 + 2S_2$ |
| $P + S_1 \overset{K_F}{\leftrightarrow} F - S_1$ | $CHOL - S_1 \overset{k_{CC}}{\longrightarrow} CHA - S_1 + H_2O$ |
| $H_2 + 2S_2 \overset{K_{H_2}}{\longleftrightarrow} 2H - S_2$ | $P - S_1 + 2H - S_2 \overset{k_{FB}}{\longrightarrow} B - S_1 + H_2O + 2S_2$ |
| | $P - S_1 + 6H - S_2 \overset{k_{FC}}{\longrightarrow} CHOL - S_1 + 6S_2$ |

A general rate expression for anisole HDO was developed considering the elementary reactions presented in Table 1, applying the assumptions made for the reaction network approached in this work (Fig. 2). The derived velocity expression for the anisole HDO reaction (Eq. 3) is:

$$(-r_A) = \left(\frac{k_A^{'} K_A C_A}{1 + \sum K_i C_i}\right)\left(\frac{\sqrt{K_{H_2} C_{H_2}}}{1 + \sqrt{K_{H_2} C_{H_2}}}\right) \qquad \text{Eq. 3}$$

Since the hydrogen concentration is higher than the amount consumed, it is assumed that the $H_2$ concentration remains constant throughout the reactor. Therefore, the last term of the above equation is considered a pseudo-constant and is defined as $k_A$, leading to Eq. 4:

$$(-r_A) = \frac{k_A K_A C_A}{1 + \sum K_i C_i}, \quad \text{where } k_A = k_A^{'}\left(\frac{\sqrt{K_{H_2} C_{H_2}}}{1 + \sqrt{K_{H_2} C_{H_2}}}\right) \qquad \text{Eq. 4}$$

Considering the assumption of a pseudo-equilibrium state and a constant and excess concentration of hydrogen in the reactor, it is possible to formulate a specific equation rate for each compound involved in the reaction scheme (equations Eq. 5 to Eq. 11). This approach allows for systematically analyzing reaction dynamics under the stated condition.

$$(-r_A) = \frac{dC_A}{dh} = -(k_{DMO} + k_{DME} + k_{HYDA}) K_A C_A [S], \text{ where } h = f(WHSV) \qquad \text{Eq. 5}$$

ISSN-e 2594-0317

$$r_B = \frac{dC_B}{dh} = (k_{DMO}K_AC_A + k_{FB}K_AC_A - k_{BC}K_BC_B)[S] \quad \text{Eq. 6}$$

$$r_P = \frac{dC_P}{dh} = (k_{DME}K_AC_A - k_{FB}K_PC_P - k_{FC}K_PC_P)[S] \quad \text{Eq. 7}$$

$$r_{MTCH} = \frac{dC_{MTCH}}{dh} = (k_{HYDA}K_AC_A - k_{MC}K_{MTCH}C_{MTCH})[S] \quad \text{Eq. 8}$$

$$r_{CHA} = \frac{dC_{CHA}}{dh} = (k_{BC}K_BC_B + k_{CC}K_{CHOL}C_{CHOL})[S] \quad \text{Eq. 9}$$

$$r_{CHA} = \frac{dC_{CHA}}{dh} = (k_{BC}K_BC_B + k_{CC}K_{CHOL}C_{CHOL})[S] \quad \text{Eq. 10}$$

$$[S] = \frac{1}{1 + K_AC_A + K_BC_B + K_PC_P + K_{MTCH}C_{MTCH} + K_{CHOL}C_{CHOL} + K_{CHA}C_{CHA}} \quad \text{Eq. 11}$$

For the calculation of the kinetic parameters, independent measurements can be performed by feeding each of the reactants (anisole, phenol, cyclohexane, benzene, and cyclohexanol) into a reactor operating at differential conversions (<15 %) varying the initial molar feed concentration to obtain significant fitting parameter s (see Table 2), which allows simplifying the expression of the reaction rate in Eq. 4 by ignoring the adsorption terms for the products and thus obtaining parameters for each reactant. Under these conditions, for any reactant *i*, Eq. 4 simplifies to:

$$(-r_i) = \frac{k_iK_iC_i}{1 + K_iC_i}, \quad \text{where} \qquad i = \{A, B, CHA, MTCH, CHOL, P\} \quad \text{Eq. 12}$$

Eq. 12 can be rearranged into the following linear expression:

$$\frac{1}{(-r_i)} = \left(\frac{1}{k_iK_i}\right)\frac{1}{C_i} + \frac{1}{k_i} \quad \text{Eq. 13}$$

By plotting $\frac{1}{(-r_i)}$ vs $\frac{1}{C_i}$, the adsorption constant $K_i$ of any reactant can be obtained from the ratio of the intersection $\frac{1}{k_i}$ and the slope $\frac{1}{k_iK_i}$ [13]. Here again, the $H_2$ term is lumped into the constant $k_i$ and does not affect the calculation of $K_i$.

The reaction rate for reactant *i* was calculated using the following equation:

$$(-r_i) = \frac{C_{i0}Q}{w}X_i \quad \text{Eq. 14}$$

$Q$ is the volumetric flow rate fed, $C_{i0}$ is the initial concentration of reactant *i*, $X_i$ is the conversion, and $w$ is the catalyst weight.

*J. Mex. Chem. Soc.* **2025**, *69*(1)
Special Issue

ISSN-e 2594-0317

**Table 2.** Experimental data for calculation of kinetic parameters.

| Reactant | $C_{i,0}$ (mol·L$^{-1}$) | Operation conditions |
|---|---|---|
| Anisole (A) | | |
| Phenol (P) | $C_{1,0}$= 0.175 | T= 300 °C |
| Cyclohexane (CHA) | $C_{2,0}$= 0.200 | $P_{H2}$= 40 bar |
| Benzene (B) | $C_{3,0}$= 0.225 | Q= 0.6 mL·min$^{-1}$ |
| Cyclohexanol (CHOL) | | |

To correctly identify the reaction products of HDO in the analysis phase, a blank reaction was conducted to sample potential reaction products between the catalyst and solvents used. For this purpose, hexadecane and dodecane were reacted separately in the presence of the Ru/$TiO_2$ catalyst.

## Results and discussion

### Catalyst characterization

X-ray powder diffraction analysis was conducted to determine the structure of the $TiO_2$ and Ru/$TiO_2$ catalyst, as shown in Fig. 3. The diffractogram revealed narrow and intense peaks related to the anatase phase (JCPDS 21-1272), along with less intense peaks corresponding to the rutile phase (JCPDS 21-1276). The identification of both anatase and rutile phases indicates a mixed-phase material, typical for commercial $TiO_2$ [41], suggesting that the bulk structure remained largely unaffected by the Ru impregnation. The absence of diffraction peaks related to the Ru phase suggests the presence of highly dispersed Ru nanoparticles (<5 nm; below the equipment detection limits), potentially facilitating a Ru-$TiO_2$ synergistic effect [36]. The $TiO_2$-anatase phase, known for its high reducibility and oxygen vacancy generation, is crucial for promoting deoxygenation reactions in the HDO reaction.

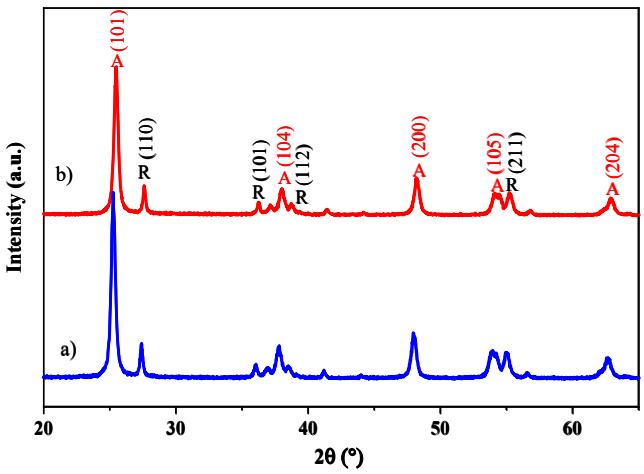


**Fig. 3.** X-ray diffraction pattern from dried materials: **(a)** $TiO_2$ and **(b)** Ru/ $TiO_2$. A: anatase, R: rutile.

*J. Mex. Chem. Soc.* **2025**, *69*(1)
Special Issue

ISSN-e 2594-0317

The TPR-$H_2$ profile for the Ru/$TiO_2$ catalyst displayed an intense sharp peak at 147 °C and a weaker peak at around 300 °C (Fig. 4.). The low-temperature peak is likely attributed to the decomposition of surface Ru-$NO_3$ species, derived from the Ru(NO)$(NO_3)_3$ precursor, and their subsequent reduction from $Ru^{3+}$→$Ru^0$ [13]. This sharp reduction signal at 147 °C suggests the formation of highly dispersed $Ru^0$ metal active sites, which are crucial for dissociative adsorption of hydrogen. The higher temperature peak may be attributed to the reduction of Ru species strongly interacting with the support, possibly forming surface defects near metal clusters, promoting the creation of adjacent oxygen vacancies. These observations reinforce the proposed L-H mechanism, where dissociative hydrogen adsorption occurs on the Ru sites, while oxygen vacancies on the $TiO_2$ support facilitate the adsorption and activation of oxygenated intermediates.

Surface acidity is a crucial property in heterogeneous catalysts for HDO reactions [36]. Therefore, TPD-$NH_3$ experiments (Fig. 5) were conducted to determine the amount and strength of acid sites in the catalyst, as shown in Table 3. The acid strength of surface sites was classified according to the $NH_3$-desorption temperature [13]: (i) weak acid sites up to 250 °C; (ii) medium acid sites between 250-400 °C; and (iii) strong acid sites, above 400 °C. The profiles showed a broad peak between 100 and 400 °C, indicating mainly weak and medium acid sites. The slight increases in the medium acid sites in the Ru/$TiO_2$ catalyst, compared to pure $TiO_2$, is attributed to the acid sites generated by the supported Ru phase, as evidenced by its TPD-$NH_3$ profiles (Fig. 5). The decrease in the number of strong acid sites on the support could result from the deposition of Ru species on these sites during impregnation, suggesting affinity of strong acid sites to adsorb Ru-$NO_3$ species during impregnation step, as previously reported by Valdés-Martínez et al. [36].Weak and medium acid sites promote the adsorption and activation of oxygenated organic compounds, like anisole [13,42], supporting the proposed competitive adsorption in the L-H model.

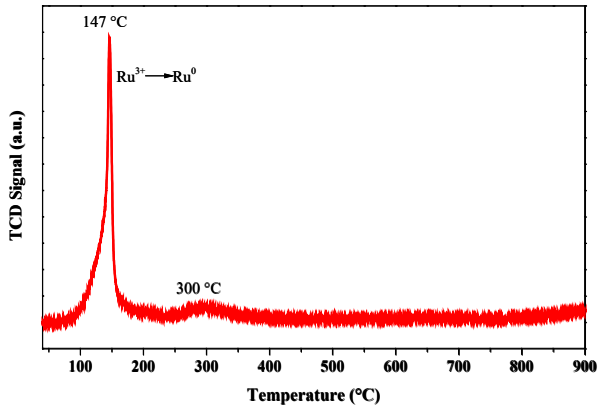


**Fig. 4**. TPR-$H_2$ profile of Ru/$TiO_2$ catalyst (dried @ 120 °C).

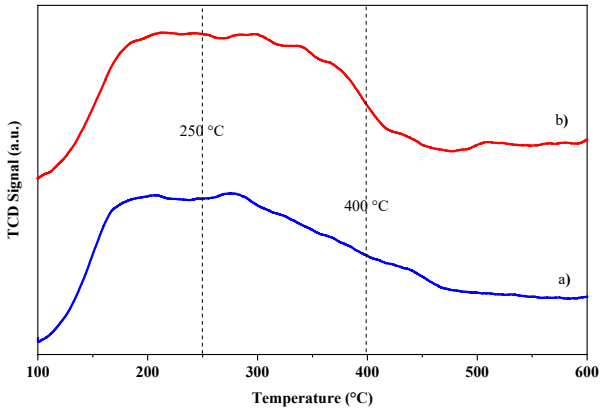


**Fig. 5.** $NH_3$-TPD profiles for **(a)** $TiO_2$ (blue) and **(b)** Ru/$TiO_2$ catalyst (red). Samples $H_2$-reduced @ 350 °C.

*J. Mex. Chem. Soc.* **2025**, *69*(1)
Special Issue

ISSN-e 2594-0317

**Table 3.** Surface acid site concentration for $TiO_2$ and $Ru/TiO_2$ materials reduced in $H_2$ at 350 °C.

| Sample | Acid sites ($\mu mol_{NH3} \cdot g_{cat}^{-1}$) | | | |
|---|---|---|---|---|
| | **Total acid sites** | **Weak (100-250 °C)** | **Medium (250-400 °C)** | **Strong (400-600 °C)** |
| $TiO_2$ | 144 | 60 | 67 | 17 |
| $Ru/TiO_2$ | 134 | 57 | 71 | 6 |

Finally, Ru 3d/C 1s and O 1s XPS spectra were obtained to determine the surface composition of Ru and O entities in the reduced $Ru/TiO_2$ catalyst (Fig. 6 and Fig. 7 , respectively). The peak at 284.8 eV is typically associated with the C 1s core level (see Fig. 6), originating from adventitious carbon and used as a reference. The Ru 3d core level peak appeared at a slightly lower binding energy (BE) than the C 1s core level, with identifiable Ru $3d_{5/2}$ and Ru $3d_{3/2}$ core levels. The peaks at 280.1 and 284.3 eV (Ru $3d_{5/2}$) correspond to $Ru^0$ species, while the peaks at 282.6 and 286.7 eV (Ru $3d_{3/2}$) are associated with residual species of the precursor species [43]. XPS results indicate that approximately 75 at.% Ru is present as a metallic phase ($Ru^0$) on the catalyst surface (Table 4). The high proportion of $Ru^0$ species confirms the availability of metallic sites necessary for hydrogen activation, as required by the kinetic model. Given that the sample was reduced at 350 °C, higher than the temperature required for Ru species reduction observed in the TPR-$H_2$ profile (Fig. 4), well-dispersed Ru particles likely formed strong interaction with the $TiO_2$ support, facilitating complete reduction during activation [44]. These $Ru^0$ sites are crucial for the dissociative adsorption of hydrogen, further supporting the model´s assumptions regarding hydrogen activation on metal sites.

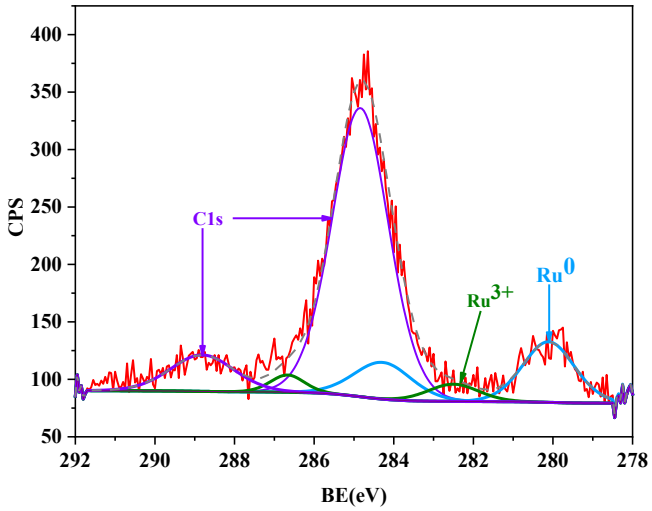


**Fig. 6.** Ru 3d/C 1s XPS spectrum of $Ru/TiO_2$ catalyst reduced in $H_2$ at 350 °C.

*J. Mex. Chem. Soc.* **2025**, *69*(1)
Special Issue

ISSN-e 2594-0317

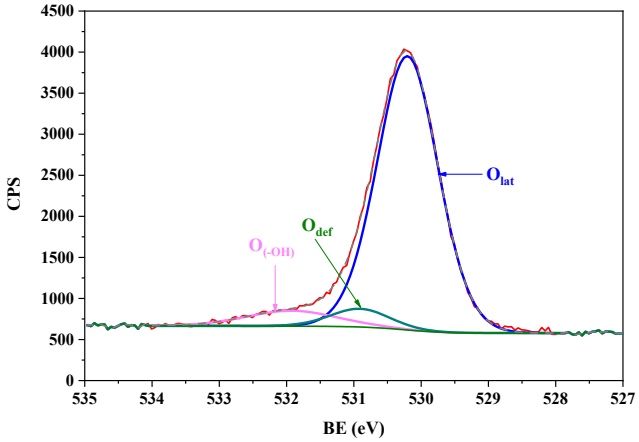


**Fig. 7.** O 1s XPS spectrum of $Ru/TiO_2$ catalyst reduced in $H_2$ at 350 °C.

Regarding the oxygen species on the catalyst, Fig. 7 shows the deconvoluted spectrum with three fingerprints identified for O species: (i) $O_{lat}$, lattice oxygen species from $TiO_2$ (530.2 eV), (ii) $O_{(-OH)}$, oxygen from surface hydroxyl groups and adsorbed water (531.9 eV), and (iii) $O_{def}$, oxygen adsorbed on surface defect-related sites on the support structure (530.9 eV), i.e. oxygen vacancies [45]. The presence of $O_{def}$ species (oxygen vacancies) is particularly important, as they facilitate the cleavage of C–O bonds to produce benzene [45], in alignment with the model's requirement for oxophilic sites that adsorb and activate oxygenated intermediates. These findings corroborate the proposed L-H model, which requires the presence of both $Ru^0$ metallic sites and oxygen vacancy to effectively catalyze the anisole HDO reaction.

**Table 4.** Surface composition and surface atomic percentage of Ru and O entities in reduced $Ru/TiO_2$ catalyst were determined by XPS.

| Ru species | Ru $3d_{5/2}$ (eV) | Ru $3d_{3/2}$ (eV) | at.% Ru | Oxygen species | O 1s | at.% O |
|---|---|---|---|---|---|---|
| $Ru^0$ | 280.1 | 284.3 | 74.2 | $O_{lat}$ | 530.2 | 87.2 |
| $Ru^{3+}$ | 282.6 | 286.7 | 25.8 | $O_{def}$ | 530.9 | 5.6 |
| | | | | $O_{(-OH)}$ | 531.9 | 7.2 |

The catalyst characterization provides experimental evidence confirming the presence of $Ru^0$ nanoparticles and oxophilic sites (oxygen vacancies and acid sites) on the $TiO_2$ support, which validates the key assumption of the Langmuir-Hinshelwood model. These dual active sites facilitate hydrogen dissociation and oxygenate adsorption, supporting the model´s prediction of competitive adsorption and reaction kinetics in the HDO of anisole.

## Catalytic evaluation

### Effect of reagent feed flow rate and temperature on anisole HDO reaction

Three experiments were conducted in a continuous packed-bed flow reactor to evaluate the effect of WHSV in the range of 2.0-20.0 $h^{-1}$ at 200, 250, and 300 °C under 40 bar $H_2$ pressure with a flow of 0.2 M anisole solution. Fig. 8 shows the first-order reaction kinetic rates for anisole HDO as a function of WHSV at different temperatures. In Fig. 8**(a)**, at 200 °C, the reaction rate presents at an initial value of $6x10^{-7}$ $mol_A \cdot (g_{CAT} \cdot s)^{-1}$ at 3.48 $h^{-1}$, and then it

*J. Mex. Chem. Soc.* **2025**, *69*(1)
Special Issue

ISSN-e 2594-0317

increases until reaching a value ~2.0x10$^{-6}$ mol$_A$·(g$_{CAT}$·s)$^{-1}$. From here on, the increase in the reaction rate becomes more noticeable and seems to become stable. The reaction rate at 250 and 300 °C (Fig. 8**(b)** and Fig. 8**(c)**) was similar to that at 200 °C, reaching rate values of 5.0x10$^{-6}$ and 7.1x10$^{-6}$ mol$_A$·(g$_{CAT}$·s)$^{-1}$, respectively. At all temperatures, the reaction rates approached an asymptotic value as the WHSV increased, showing direct proportionality with the anisole feed flow. This behavior suggests that at higher WHSV values, greater than 14.0 h$^{-1}$, the reaction is controlled by intrinsic kinetic rather than external mass transfer limitations, confirming the kinetic model's assumption that reaction rate depends on surface phenomena.

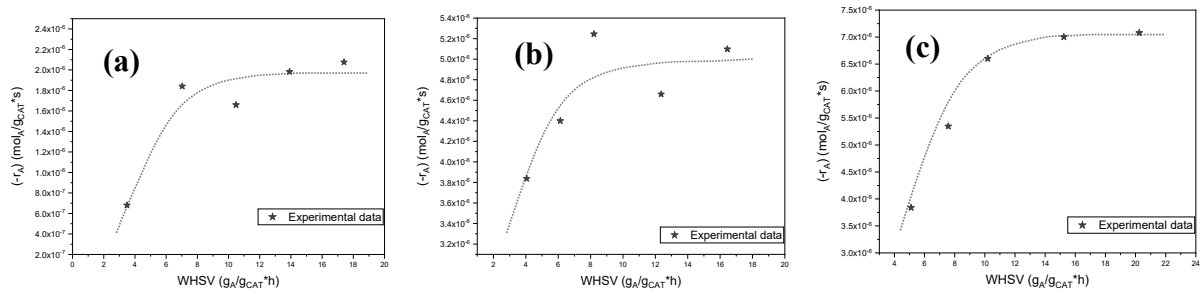


**Fig. 8.** First-order reaction kinetic rates for anisole HDO at **(a)** 200, **(b)** 250, and **(c)** 300 °C as a function of WHSV (P$_{H2}$, 40 bar).

Anisole conversion is a function of WHSV; as WHSV increases, the contact time between the reactive mixture and the catalyst decreases, leading to a decrease in anisole conversion. Based on this consideration, the response of anisole conversion at various WHSV and temperatures was studied. The experimental selectivity of the anisole HDO reaction pathways was plotted as a function of temperature (Fig. 9-a) to identify favorable reaction temperature for the formation of B. It was observed that at 300 °C, the formation of undesirable oxygenated by-products such as MTCH, CHOL, and P was minimized, with only two main products: B and CHA.

At 300 °C, the formation of the desired products, benzene, and cyclohexane, was favored across the WHSV range, indicating a preference for the demethoxylation (DMO) route. At low conversion (<0.2), the yield of B and CHA were nearly the same; however, at conversions around 0.35, the yield of CHA was five times higher than that of B. This observation suggests that the deoxygenation pathway via demethoxylation (DMO) is predominant under these conditions, aligning with the kinetic model´s assumption that anisole adsorbs on oxophilic sites and reacts preferentially through the DMO pathway. To optimize $H_2$ consumption, 300°C is the ideal reaction temperature to achieve the maximum catalytic conversion and to nullify the formation of unwanted oxygenated products, predominantly forming B and CHA. Fig. 9-b shows the dependence of the B/CHA yield ratio as a function of WHSV, with an optimum value of B/CHA at WHSV= 15.3 h$^{-1}$.

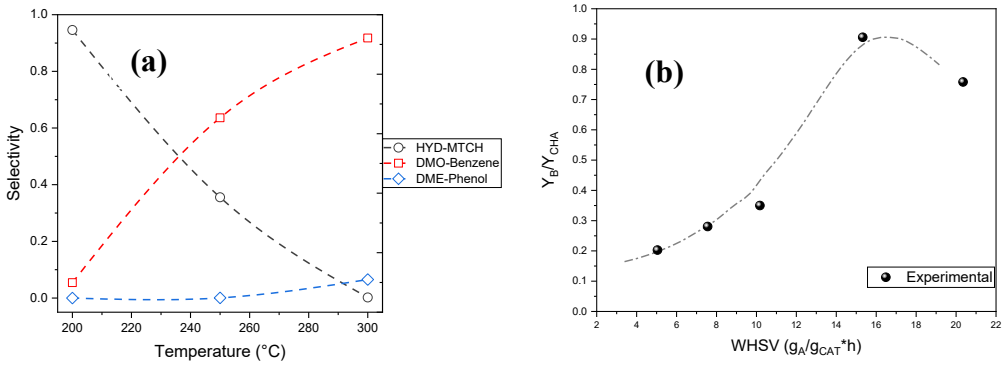


**Fig. 9.** Representative profiles for the anisole HDO reaction: **(a)** HYD, DMO, and DME selectivity as a function of reaction temperature; and **(b)** B/CHA yield ratio as a function of WHSV. Operation conditions: 300 °C and 40 bar ($H_2$).

ISSN-e 2594-0317

### Effect of hydrogen pressure on anisole HDO

Three experiments were conducted by varying the total $H_2$ pressure (30-50 bar), keeping the temperature and WHSV fixed (300 °C and 15.3 $h^{-1}$; 0.2 M anisole feed flow). The molar fraction of hydrogen in the liquid phase and the $H_2$/anisole molar ratio at the reaction conditions are shown in Table 5.

**Table 5.** Dissolved hydrogen fraction and $H_2$/anisole molar ratio in liquid-phase as the $H_2$ partial pressure.

| Experiment | $P_{H2}$ (bar) | $X_{liq}$ $H_2$ | $H_2$/anisole (mol/mol) |
|---|---|---|---|
| 1 | 30 | 0.0737 | 6.93 |
| 2 | 40 | 0.0968 | 9.09 |
| 3 | 50 | 0.1186 | 11.14 |

* Anisole in the vapor phase was neglected.

The evaluation of the anisole conversion and its reaction rate as a function of $H_2$ pressure indicates that at 300 °C, anisole conversion primarily depends on the contact time between the reactive mixture and the catalyst within the pressure range studied, which is consistent with the kinetic model´s assumption that hydrogen concentration influences the reaction rate. Conversely, Ghampson et al. [15] did not observe relevant changes when modifying the $H_2$ pressure in a batch reactor using the Re-$MoO_x$/$TiO_2$ catalyst. However, the selectivity of the reaction was influenced by the amount of $H_2$ dissolved in the solution; a higher amount of dissolved hydrogen led to increased hydrogenation of the aromatic ring due to the availability of $H_2$ [46,47], generating mainly benzene, cyclohexane, and phenol. When correlating these findings with the data in Table 5, it is clear that the amount of $H_2$ dissolved in the liquid phase influenced only the selectivity of anisole HDO (double bond saturation rate) but not the catalytic activity (deoxygenation rate). $H_2$ pressures of 30 bar yielded a B/CHA ratio close to unity, while $P_{H2}$= 50 bar, a CHA/B ratio of 3.5 was obtained. This result supports the kinetic model´s consideration of hydrogen pressure affecting the hydrogenation steps in the reaction mechanism.

### Parameter estimation and kinetic model validation in a differential reactor

### Parameter estimation in differential reactor

Considering the optimized pressure and temperature values (40 bar and 300 °C), the reaction was further evaluated by varying the feed of the products A, B, CHA, P, and CHOL, thus adjusting the WHSV while operating in a differential conversion regime. Kinetic and adsorption constants were estimated by linear regression of Eq. 13, derived from the proposed L-H model, and the results are summarized in Table 6. The good agreement between the experimental data and the model predictions validates the applicability of the L-H model for anisole HDO over Ru/$TiO_2$. The data show that B and CHOL are the most strongly adsorbed species. The fastest-reacting compounds were CHOL, and P. CHOL has a kinetic constant of 2.8 times that of anisole, while P is 2.2 times that of anisole. These values explain why, at 300°C, the observed yields of P and CHOL were significantly lower than B, as they react more rapidly, which is consistent with kinetic model predictions.

*J. Mex. Chem. Soc.* **2025**, *69*(1)
Special Issue

ISSN-e 2594-0317

**Table 6.** Kinetic and equilibrium constants for the HDO reaction pathway derived from experimental data fit.

| **Compound** | **Adsorption constant, *K* (L·mol$^{-1}$)** | **Reaction constant, *k* (x10$^6$ mol•(g$_{CAT}$·s)$^{-1}$)** | **r$^2$** |
|---|---|---|---|
| Anisole | 9.2 ± 1.2 | 13.05 ± 1.53 | 0.95 |
| Benzene | 21.0 ± 1.6 | 7.51 ± 0.62 | 0.99 |
| Phenol | 14.3 ± 0.7 | 28.82 ± 1.63 | 0.98 |
| Cyclohexanol | 24.3 ± 1.4 | 35.84 ± 1.96 | 0.96 |
| Cyclohexane | 12.0 ± 0.4 | 0.02 ± 0.0003 | 0.99 |

## Model validation

The L-H kinetic model considering two adjacent active site types was proposed to describe the anisole HDO reaction. The equations Eq. 5-Eq. 11 were simultaneously solved using Polymath V6.1 software. Fig. 10 shows experimental anisole concentration values as a function of WHSV, where the kinetic model fits the experimental data obtained for the anisole HDO reaction using the Ru/$TiO_2$ catalyst well. The percentage deviation between the experimental and predicted values is shown in Fig. 10, with an average deviation of ~5.0%, demonstrating good agreement and validating the model´s applicability to this system.

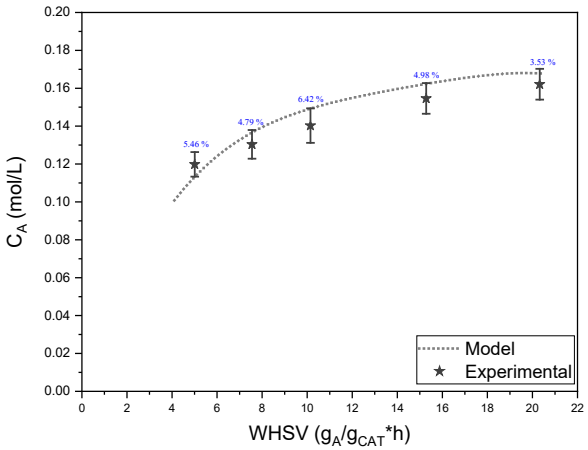


**Fig. 10.** Comparison of kinetic model prediction and experimental data for anisole concentration as a function of WHSV. Operation conditions: 300 °C and 40 bar $H_2$.

Fig. 11 illustrates the anisole reaction network at 300 °C, using the estimated kinetic parameters for each reaction step, derived from the overall reaction constants presented in Table 6. The results indicate that the ratio $k_{DMO}/k_{DME}$ is 3.5, suggesting that the DMO pathway is favored over the DME pathway, which aligns with the experimental observations and supports the model´s assumptions. Additionally, it is observed that the conversion of CHOL to CHA is the fastest reaction step, which explains why CHOL was barely detectable in the product quantification.

*J. Mex. Chem. Soc.* **2025**, *69*(1)
Special Issue

ISSN-e 2594-0317

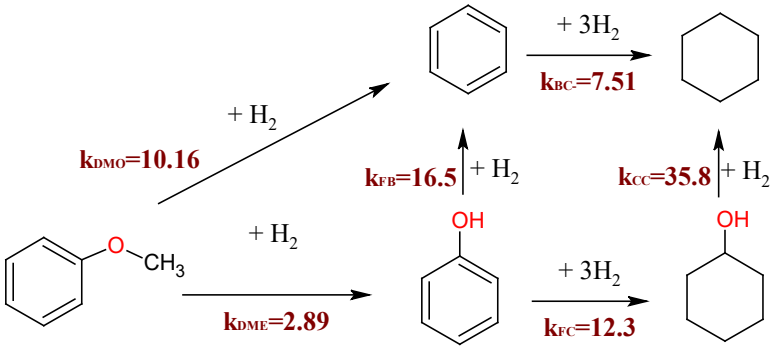


**Fig. 11.** Anisole reaction pathway with kinetic constants (x$10^{-6}$ mol•($g_{CAT}$·s)$^{-1}$) derived from the proposed L-H kinetic model at 300°C.

The validation of the method was crucial as it allowed for a reliable approximation of the reaction mechanism and the determination of kinetic parameters for predicting reactions under established pressure and temperature conditions with the Ru/$TiO_2$ catalyst. The characterization results support the proposed two-site model for the anisole HDO reaction by identifying highly dispersed metallic $Ru^0$ and oxophilic sites, including acidic sites and oxygen vacancies. Metallic sites facilitate hydrogen activation, while oxophilic sites assist in oxygenate adsorption and activation. This dual functionality aligns with the Langmuir-Hinshelwood kinetic model and is validated by the close fit between the model predictions and the experimental data. As evidenced by characterization results, the well-dispersed active $Ru^0$ sites, along with acid sites and oxygen-affinity sites on the catalytic surface, were key to the high conversion of anisole to aromatic and cyclic deoxygenated products at 300 °C and 30 bar. At 300 °C, the properties of this catalyst facilitate effective adsorption and reaction of oxygenated molecules, leading to higher yields of benzene and cyclohexane.

## Conclusions

The kinetic regime for anisole hydrodeoxygenation was confirmed at WHSV values ≥ 14.0 $h^{-1}$, effectively minimizing external mass transfer limitations. The reaction rate was found to be independent of the anisole feed concentration and primarily governed by surface reaction kinetics. At 300 °C, the yield of deoxygenation compounds exceeded 95 %, with benzene and cyclohexane as the primary products. The benzene-to-cyclohexane (B/CHA) ratio was strongly influenced by the contact time, reaching a maximum at WHSV=15.3 $h^{-1}$. The proposed Langmuir-Hinshelwood kinetic model fits well with the experimental data, indicating a preference for the demethoxylation (DMO) over the demethylation (DME) pathway. The conversion of cyclohexanol to cyclohexane was identified as the fastest reaction step. Cyclohexanol exhibits the highest chemisorption and reactivity on the catalyst surface, followed by phenol, leading to a higher yield of deoxygenation products. Surface acid and oxygen defect sites ($O_{def}$) were found to enhance deoxygenation rates.

This study successfully validates the Langmuir-Hinshelwood kinetic model for the anisole HDO over the Ru/$TiO_2$ catalyst. Catalyst characterization confirmed the presence of both metallic $Ru^0$ sites and oxophilic sites, which are crucial for the dual-site mechanism proposed. The close agreement between the model predictions and the experimental data validates the model´s accuracy and reliability, providing a solid framework for optimizing and scaling up the HDO process for industrial applications.

ISSN-e 2594-0317

## Acknowledgments

Thanks are due to CONAHCYT-México for funding through project CB-A1-S-41193 and PRONACES-321073. V.M.J., R.R.E., and J.G.F. acknowledge CONAHCYT-México for financial support through graduated student scholarships (707700 and 788372) and the postdoc grant (687839). V.A.S.-T. thanks to the IxM-CONAHCYT Program (Project CIR/0064/2022). We acknowledge to Dra. E. Gordillo and L. Huerta from IIM-UNAM for XPS analyses. We acknowledge the valuable comments of the reviewers to improve this paper.

## References

1. Lange, J. P. *Biofuels Bioprod. Biorefin.* **2007**, *1*, 39-48. DOI: https://doi.org/10.1002/bbb.7.
2. Choudhary, T. V.; Phillips, C. B. *Appl. Catal., A* **2011,** *397*, 1-12. DOI: https://doi.org/10.1016/j.apcata.2011.02.025.
3. Furimsky, E. *Catal. Today* **2013,** *217*, 13-56. DOI: https://doi.org/10.1016/j.cattod.2012.11.008.
4. Furimsky, E. *Appl. Catal., A* **2000,** *199*, 147-190. DOI: https://doi.org/10.1016/s0926-860x(99)00555-4.
5. McKendry, P. *Bioresour. Technol.* **2002,** *83*, 37-46. DOI: https://doi.org/10.1016/s0960-8524(01)00118-3.
6. Bu, Q.; Lei, H.; Zacher, A. H.; Wang, L.; Ren, S.; Liang, J.; Wei, Y.; Liu, Y.; Tang, J.; Zhang, Q.; Ruan, R. *Bioresour. Technol.* **2012,** *124*, 470-7. DOI: https://doi.org/10.1016/j.biortech.2012.08.089.
7. Elliott, D. C. *Energy Fuels* **2007,** *21*, 1792-1815. DOI: https://doi.org/10.1021/ef070044u.
8. Wang, H.; Male, J.; Wang, Y. *ACS Catal.* **2013,** *3*, 1047-1070. DOI: https://doi.org/10.1021/cs400069z.
9. Badawi, M.; Paul, J. F.; Cristol, S.; Payen, E.; Romero, Y.; Richard, F.; Brunet, S.; Lambert, D.; Portier, X.; Popov, A.; Kondratieva, E.; Goupil, J. M.; El Fallah, J.; Gilson, J. P.; Mariey, L.; Travert, A.; Maugé, F. *J. Catal.* **2011,** *282*, 155-164. DOI: https://doi.org/10.1016/j.jcat.2011.06.006.
10. Weigold, H. *Fuel* **1982**, *61*, 1021-1026. DOI: https://doi.org/10.1016/0016-2361(82)90104-1.
11. Odebunmi, E. *J. Catal.* **1983,** *80*, 56-64. DOI: https://doi.org/10.1016/0021-9517(83)90229-4.
12. Wandas, R.; Surygala, J.; Śliwka, E. *Fuel* **1996,** *75*, 687-694. DOI: https://doi.org/10.1016/0016-2361(96)00011-7.
13. Valdés-Martínez, O. U.; Suárez-Toriello, V. A.; Reyes, J. A. D. L.; Pawelec, B.; Fierro, J. L. G. *Catal. Today* **2017,** *296*, 219-227. DOI: https://doi.org/10.1016/j.cattod.2017.04.007.
14. Sorensen, B.; Spazzafumo, G. in: *Hydrogen and Fuel Cells*. 2nd ed.; Elsevier Science: 2012; 501. DOI: https://doi.org/10.1016/c2009-0-63881-2.
15. Nie, L.; Resasco, D. E. *J. Catal.* **2014,** *317*, 22-29. DOI: https://doi.org/10.1016/j.jcat.2014.05.024.
16. Ballesteros-Plata, D.; Infantes-Molina, A.; Rodríguez-Cuadrado, M.; Rodríguez-Aguado, E.; Braos-García, P.; Rodríguez-Castellón, E. *Appl. Catal., A* **2017,** *547*, 86-95. DOI: https://doi.org/10.1016/j.apcata.2017.08.034.
17. Yang, F. F.; Liu, D.; Wang, H.; Liu, X.; Han, J. Y.; Ge, Q. F.; Zhu, X. L. *J. Catal.* **2017,** *349*, 84-97. DOI: https://doi.org/10.1016/j.jcat.2017.01.001.
18. Zhu, X.; Nie, L.; Lobban, L. L.; Mallinson, R. G.; Resasco, D. E. *Energy Fuels* **2014,** *28*, 4104-4111. DOI: https://doi.org/10.1021/ef500768r.
19. Zhong, Z.; Li, J.; Jian, M.; Shu, R.; Tian, Z.; Wang, C.; Chen, Y.; Shi, N.; Wu, Y. *Fuel* **2023,** *333*. DOI: https://doi.org/10.1016/j.fuel.2022.126241.

*J. Mex. Chem. Soc.* **2025**, *69*(1)
Special Issue

ISSN-e 2594-0317

20. Newman, C.; Zhou, X.; Goundie, B.; Ghampson, I. T.; Pollock, R. A.; Ross, Z.; Wheeler, M. C.; Meulenberg, R. W.; Austin, R. N.; Frederick, B. G., *Appl. Catal., A* **2014,** *477*, 64-74. DOI: https://doi.org/10.1016/j.apcata.2014.02.030.
21. Shu, R.; Lin, B.; Zhang, J.; Wang, C.; Yang, Z.; Chen, Y. *Fuel Process. Technol.* **2019,** *184*, 12-18. DOI: https://doi.org/10.1016/j.fuproc.2018.11.004.
22. Zhong, Z.; Luo, B.; Lin, C.; Yin, T.; Tian, Z.; Wang, C.; Chen, Y.; Wu, Y.; Shu, R. *Fuel* **2023,** *340*. DOI: https://doi.org/10.1016/j.fuel.2023.127567.
23. Boonyasuwat, S.; Omotoso, T.; Resasco, D. E.; Crossley, S. P. *Catal. Lett.* **2013,** *143*, 783-791. DOI: https://doi.org/10.1007/s10562-013-1033-3.
24. Anex, R. P.; Aden, A.; Kazi, F. K.; Fortman, J.; Swanson, R. M.; Wright, M. M.; Satrio, J. A.; Brown, R. C.; Daugaard, D. E.; Platon, A.; Kothandaraman, G.; Hsu, D. D.; Dutta, A. *Fuel* **2010,** *89* (SUPPL. 1), S29-S35. DOI: https://doi.org/10.1016/j.fuel.2010.07.015.
25. 25. Kim, H.; Yang, S.; Lim, Y. H.; Lee, J.; Ha, J.-M.; Kim, D. H. *J. Catal.* **2022,** *410*, 93-102. DOI: https://doi.org/10.1016/j.jcat.2022.04.017.
26. de Souza, P. M.; Rabelo-Neto, R. C.; Borges, L. E. P.; Jacobs, G.; Davis, B. H.; Graham, U. M.; Resasco, D. E.; Noronha, F. B. *ACS Catal.* **2015,** *5*, 7385-7398. DOI: https://doi.org/10.1021/acscatal.5b01501.
27. Dinh Ngo, S.; Tuong Vi Tran, T.; Kongparakul, S.; Reubroycharoen, P.; Kidkhuntod, P.; Chanlek, N.; Wang, J.; Guan, G.; Samart, C. *J Anal Appl Pyrolysis* **2020,** *145*. DOI: https://doi.org/10.1016/j.jaap.2019.104745.
28. Lee, W. S.; Wang, Z. S.; Wu, R. J.; Bhan, A. *J. Catal.* **2014,** *319*, 44-53. DOI: https://doi.org/10.1016/j.jcat.2014.07.025.
29. Berger, R. J.; Stitt, E. H.; Marin, G. B.; Kapteijn, F.; Moulijn, J. A. *Cattech.* **2001,** *5*, 36-60. DOI: https://doi.org/10.1023/a:1011928218694.
30. Ghampson, I. T.; Canales, R.; Escalona, N. *Appl. Catal., A* **2018,** *549*, 225-236. DOI: https://doi.org/10.1016/j.apcata.2017.10.009.
31. Li, Y.; Fu, J.; Chen, B., *RSC Adv.* **2017,** *7*, 15272-15277. DOI: https://doi.org/10.1039/c7ra00989e.
32. Phan, T. N.; Ko, C. H. *Catal. Today* **2018,** *303*, 219-226. DOI: https://doi.org/10.1016/j.cattod.2017.08.025.
33. Leiva, K.; Sepulveda, C.; García, R.; Laurenti, D.; Vrinat, M.; Geantet, C.; Escalona, N. *Appl. Catal., A* **2015,** *505*, 302-308. DOI: https://doi.org/10.1016/j.apcata.2015.08.010.
34. Sitthisa, S.; Sooknoi, T.; Ma, Y. G.; Balbuena, P. B.; Resasco, D. E. *J. Catal.* **2011,** *277*, 1-13. DOI: https://doi.org/10.1016/j.jcat.2010.10.005.
35. Kunz, L.; Maier, L.; Tischer, S.; Deutschmann, O. in: *Modeling and Simulation of Heterogeneous Catalytic Reactions*, Deutschmann, O., Ed. 2011; 113-148. DOI: https://doi.org/10.1002/9783527639878.ch4.
36. Valdés-Martínez, O. U.; Díaz de León, J. N.; Santolalla, C. E.; Talavera-López, A.; Avila-Paredes, H.; de los Reyes, J. A. *Ind. Eng. Chem. Res.* **2021,** *60*, 18880-18890. DOI: https://doi.org/10.1021/acs.iecr.1c03058.
37. Valdés-Martínez, O. U.; Santolalla-Vargas, C. E.; Santes, V.; de los Reyes, J. A.; Pawelec, B.; Fierro, J. L. G. *Catal. Today* **2019,** *329*, 149-155. DOI: https://doi.org/10.1016/j.cattod.2018.11.007.
38. Kato, T.; Usami, T.; Tsukada, T.; Shibata, Y.; Kodama, T. *J. Nucl. Mater.* **2016,** *479*, 123-129. DOI: https://doi.org/10.1016/j.jnucmat.2016.06.052.
39. Granados Fócil, A. A.; Granados Fócil, S.; Conde Sotelo, V. M.; Grimm, R. L.; González García, F.; Rojas Santiago, E.; Santolalla Vargas, C. E.; Vera Ramírez, M. A.; de los Reyes Heredia, J. A. *Energy Technol.* **2019,** *7*. DOI: https://doi.org/10.1002/ente.201801112.

*J. Mex. Chem. Soc.* **2025**, *69*(1)
Special Issue

ISSN-e 2594-0317

40. Vannice, M. A. *J. Catal.* **1976,** *44*, 152-162. DOI: https://doi.org/10.1016/0021-9517(76)90384-5.
41. Wang, F.; Zhang, S.; Li, C.; Liu, J.; He, S.; Zhao, Y.; Yan, H.; Wei, M.; Evans, D. G.; Duan, X. *RSC Adv.* **2014,** *4*. DOI: https://doi.org/10.1039/c3ra47076h.
42. Popov, A.; Kondratieva, E.; Goupil, J. M.; Mariey, L.; Bazin, P.; Gilson, J.-P.; Travert, A.; Maugé, F. *J. Phys. Chem. C.* **2010,** *114*, 15661-15670. DOI: https://doi.org/10.1021/jp101949j.
43. Morgan, D. J. *Surf. Interface Anal.* **2015,** *47*, 1072-1079. DOI: https://doi.org/10.1002/sia.5852.
44. Kumar, V. P.; Beltramini, J. N.; Priya, S. S.; Srikanth, A.; Bhanuchander, P.; Chary, K. V. R. *Appl. Petrochem. Res.* **2015,** *6*, 73-87. DOI: https://doi.org/10.1007/s13203-015-0136-8.
45. Phan, T. N.; Park, Y.-K.; Lee, I.-G.; Ko, C. H. *Appl. Catal., A* **2017,** *544*, 84-93. DOI: https://doi.org/10.1016/j.apcata.2017.06.029.
46. Robinson, A. M.; Hensley, J. E.; Medlin, J. W. *ACS Catal.* **2016,** *6*, 5026-5043. DOI: https://doi.org/10.1021/acscatal.6b00923.
47. Bui, V. N.; Laurenti, D.; Delichère, P.; Geantet, C. *Appl. Catal. B Environ.* **2011,** *101*, 246-255. DOI: https://doi.org/10.1016/j.apcatb.2010.10.031.